Electrochimica Acta 113 (2013) 141–148

Contents lists available at ScienceDirect

Electrochimica Acta

journal homepage: www.elsevier.com/locate/electacta

Layered sodium titanate nanostructures as a new electrode for high energy density supercapacitors

Radhiyah Abd Aziz[a], Izan Izwan Misnon[a], Kwok Feng Chong[a], Mashitah M. Yusoff[a,b], Rajan Jose[a,*]

[a] Nanostructured Renewable Energy Materials Laboratory, Faculty of Industrial Sciences & Technology, Universiti Malaysia Pahang, 26300 Kuantan, Pahang, Malaysia
[b] Central Laboratory, Universiti Malaysia Pahang, 26300 Kuantan, Pahang, Malaysia

ARTICLE INFO

Article history:
Received 5 June 2013
Received in revised form
18 September 2013
Accepted 22 September 2013
Available online 8 October 2013

Keywords:
Alkali titanates
Electrochemistry
Energy storage
Renewable energy
Supercapacitor

ABSTRACT

A flower-shaped hydrated layered sodium titanate material, $Na_2Ti_2O_4(OH)_2$, have been synthesized through a facile hydrothermal method and subsequently converted into sodium free titania (anatase). Potential application of the $Na_2Ti_2O_4(OH)_2$ as an electrode for supercapacitors under pseudo-capacitance storage mode is evaluated. The $Na_2Ti_2O_4(OH)_2$ showed sixfold higher specific capacitance ($C_S \sim 300\ F\ g^{-1}$) in an aqueous electrolyte than the anatase and demonstrated stable electrochemical cycling. This high C_S is originated from a combination of electrochemical double layer and pseudo-capacitance storage mechanisms. The presence of hydrated layered within some loose interlayer plays an important role in assisting the diffusion process of ions as confirmed in electrical impedance spectroscopy analysis.

1. Introduction

A fast-growing market of portable electronic devices and hybrid electric vehicles (HEVs) is motivating intensive search for electrical energy storage devices characterized by high energy density ($\geq 5\ Wh\ kg^{-1}$) and power density ($\geq 10\ kW\ kg^{-1}$) [1–3]. Supercapacitors, in which the charge storage results from an electrical double layer as well as an electrochemical reaction, represent a unique class of technology with niche applications. Supercapacitors have much larger specific capacitance ($\times$20–200) and energy storage density ($\times$100) than conventional capacitors and deliver energy at a higher rate ($\times 10^3$) and stable cycle life ($>10^5$) than conventional batteries [1–3]. However, their applications are restricted by their limited energy density compared to that of lithium ion batteries. Supercapacitors store electrical energy via accumulation of electric charges at an electrical double layer (EDLC) formed at an interface between a polarizable electrode and an electrolyte. No electron transfer takes place across the electrode interface during its operation; and therefore, this charge storage process is non-Faradaic. Other than non-Faradaic charge storage process, there is Faradaic charge storage process in supercapacitors which involves a redox reaction at the electrode surface, termed pseudo-capacitance. Integration of both storage mechanisms into a single device yields higher energy storage capability [4–8]. Carbon structures such as activated carbon and carbon nanotubes are commercial choices to build supercapacitors [9,10]. Recently, ceramic nanostructures [11–14] and conducting polymers [15–17] are gaining interest as electrode materials in supercapacitors because the pseudo-capacitance also contributes to the energy storability in addition to the double layer capacitance.

Significant efforts are devoted to designing nanostructured ceramic electrode materials with high surface area and short diffusion paths for supercapacitor applications, a brief account of which are available in recent reviews [1–3,11]. Three dimensional such as flowers and mesoporous structures could possibly contribute to specific capacitance because of the opportunities for improved electrode–electrolyte interaction due to efficient penetration of electrolytes into the entire electrode matrix [18–22]. Of particular interests are materials with layered structures due to their unique structural and electrical properties [20,21,23].

Alkali titanates are a series of compounds with the formula $A_2Ti_nO_{2n+1}$ (A = Li, K, Na), characterized by large specific surface area as well as unique layered ($3 < n < 5$) and tunnel ($6 \leq n \leq 8$) crystalline structures [24–28]. These titanates could potentially be candidates as electrode materials in supercapacitors for a number of reasons including (i) layered morphology can accommodate the

* Corresponding author. Tel.: +60 9 5492451; fax: +60 9 5492766.
E-mail addresses: rjose@ump.edu.my, joserajan@gmail.com (R. Jose).

0013-4686/$ – see front matter © 2013 Elsevier Ltd. All rights reserved.
http://dx.doi.org/10.1016/j.electacta.2013.09.128

charges and allow them to diffuse only a short distance to reach the interlayer position; (ii) alkali ions existing in the interlayer space between the titanate layers carry negative charges and can be exchanged with other cations; and (iii) are able to tolerate structure strain caused by the intercalation process of ions due to the layered structure thereby improving the cycle stability [29]. Several syntheses procedures are reported for alkali titanates to produce diverse morphologies such as nanotubes and nanowires [30–33]. Typically, hydrothermal treatment of titanium precursors in highly alkaline media (e.g., NaOH and KOH) is a viable method to prepare them [33]. Nanotubes and nanorods of sodium titanates prepared via the hydrothermal route using NaOH are shown to have desirable electrochemical performance for energy storage devices such as sodium-ion batteries [29]. To the best of our knowledge, there are only a few reports on the synthesis of sodium titanate with nanoflowers structure such as electrochemical spark discharge spallation (ESDP) [34–45] and hydrothermal routes [36]. Although a template-free synthetic route, the ESDP has limitations on mass production. On the other hand, hydrothermal route is scalable and diverse morphologies could be produced by controlling the chemistry of the precursor solution.

Herein, we report a template-free and cost-effective method to synthesize layered sodium titanate hydrate with flower-like morphology facilely. The sodium titanate flowers thus synthesized showed an order of magnitude higher energy storage capacity compared to that of the TiO_2 nanoflowers obtained through a similar procedure. We have shown that water of crystallization and the cation (Na^+) residing between the edge-shared TiO_6 octahedral that stabilizes the layered sodium titanate hydrate structure contribute to its enhanced electrochemical performance.

2. Experimental procedures

2.1. Materials synthesis

Analytical reagent grade NaOH (R&M Chemicals, India), titanium tetra isopropoxide (TTIP) (Acros Organic, Germany) and methanol were the starting materials. Sodium titanate nanoflowers (STNFs) were synthesized via hydrothermal reaction between NaOH and a mixture of TTIP and methanol. In a typical synthesis, methanol (50 ml) was added to TTIP (3.0 g) and then heated up to ~67 °C with stirring. The above solution was hydrolyzed using distilled water (0.72 g) and subsequently heated for 30 min. Upon completion of the hydrolysis, NaOH (20 ml, 5 wt%) solution was added to the mixture which was then transferred to a Teflon-lined autoclave. The hydrothermal reaction was carried out at 80 °C (STNF80C) and 120 °C (STNF120C) for 24 h. Upon completion of the hydrothermal reaction, the precipitate was filtered and washed with distilled water until pH ~9–10 was attained. For Na free TiO_2, the STNF80C and the STNF120C samples were washed with 0.1 M HCl followed by distilled water until pH ~4 was obtained and subsequently dried at 70 °C for 1 h. The dried sample powder was then calcined at 500 °C for 3 h.

2.2. Materials characterization

The crystal structure of the material was studied by X-ray diffraction (XRD) technique using the Rigaku Miniflex II X-ray diffractometer employing Cu Kα radiation (λ = 1.5406 Å). The particulate properties of the materials were studied by gas-adsorption technique (Micromeritics, Model ASAP2020, USA). Morphology and microstructure of the materials were studied by scanning and transmission electron microscopic techniques. The shape and size of the samples were obtained using a field emission scanning electron microscope (FESEM, LEO 1525, ZWL, Germany). Crystal structural details of the new materials were obtained from transmission electron microscopy (TEM) was carried out with Tecnai 20 (FEI, USA) operating at 200 kV accelerated voltage.

2.3. Device fabrication and testing

For electrochemical evaluation, a working electrode was prepared by mixing the active material with polyvinylidene fluoride (PVDF) (Sigma–Aldrich, USA) and carbon black (Super P conductive, Alfa Aesar, UK) in a mass ratio of 85:5:10 and was stirred in N-methyl-2-pyrrolidinone to achieve a homogeneous mixture. The resulting slurry was then pasted on a nickel foam substrate (current collector) and the electrode was dried at 70 °C for 12 h. The dried electrode was then pressed using a pelletizer at 5 ton. A three electrode system was used to evaluate the electrochemical performance by cyclic voltammetry (CV) using a potentiostat (Autolab PGSTAT 30, Eco Chemie B.V., The Netherlands) employing NOVA 1.9 software in 1 M KOH aqueous electrolyte at room temperature. A platinum rod and a saturated Ag/AgCl electrode were used as the counter and the reference electrodes, respectively. The supercapacitive performances of the samples were evaluated from the galvanostatic charge–discharge curves in the potential range of 0–0.5 V at different current densities (1, 3, 5, 7 and 10 A g^{-1}) in 1 M KOH electrolyte. Galvanostatic cycling stability experiments were performed in the potential range of 0–0.5 V at current density 3 A g^{-1} in 1 M KOH solution for 1000 cycles. The kinetics at the electrode were studied using electrochemical impedance spectroscopy (EIS) using the Autolab Potentiostat.

3. Results and discussion

The mechanism of formation of sodium titanate from a TiO_2 sol and NaOH solution by hydrothermal process is fairly obvious. The TiO_2, being an amphoteric oxide, involves in chemical reaction as an acid or base depending on the pH of the solution [37]. The TiO_2 sol formed during refluxing the hydrolyzed TTIP reacts with NaOH as an acid to form disordered sodium titanate which grows in hydrothermal conditions into crystals. Thermogravimetric results of the hydrothermal product showed a single step weight loss of ~20% (see Supporting information, S1) at ≤200 °C. This weight loss is assigned to the liberation of adsorbed moisture. Chemical analysis of the sample revealed the following composition: Ti ~19.89%, Na ~7.51%, and O ~69.28% (see Supporting information, S2). No change in the chemical composition was observed even when the sample was heated until 800 °C from which we infer that the hydrothermal product is layered sodium titanate.

The different magnification of FESEM images for STNF80 (Fig. 1a and b) and STNF120 (Fig. 1c) showed flower-like aggregates morphology; the formation mechanism of which could be understood as follows. The TiO_2 nanoparticles formed during hydrothermal reaction undergo delamination process under the alkaline (NaOH) treatment and produce single layers of TiO_2 nanosheets [38]. High surface-to-volume ratio of these layers makes them unstable leading their edges to curl up for releasing the excess surface energy thereby forming the nanopetals. The nanosheet of each petals branched out from one another creating a floral pattern similar to a marigold or carnation. The micrometer-sized (size ~2.5 μm) nanoflower was assembled by ultrathin nanosheets growing outside from a mutual central zone of each individual spherical particle TiO_2. This tiny flower-like structure composed of petals whose thickness measured from TEM was ~20–30 nm. However, the FESEM images show that growth of STNF80C (Fig. 1b) into nanoflowers is not fully completed compared to the STNF120C (Fig. 1c) because of the presence of a larger amount of water molecules in the structure at lower temperatures (<100 °C). During

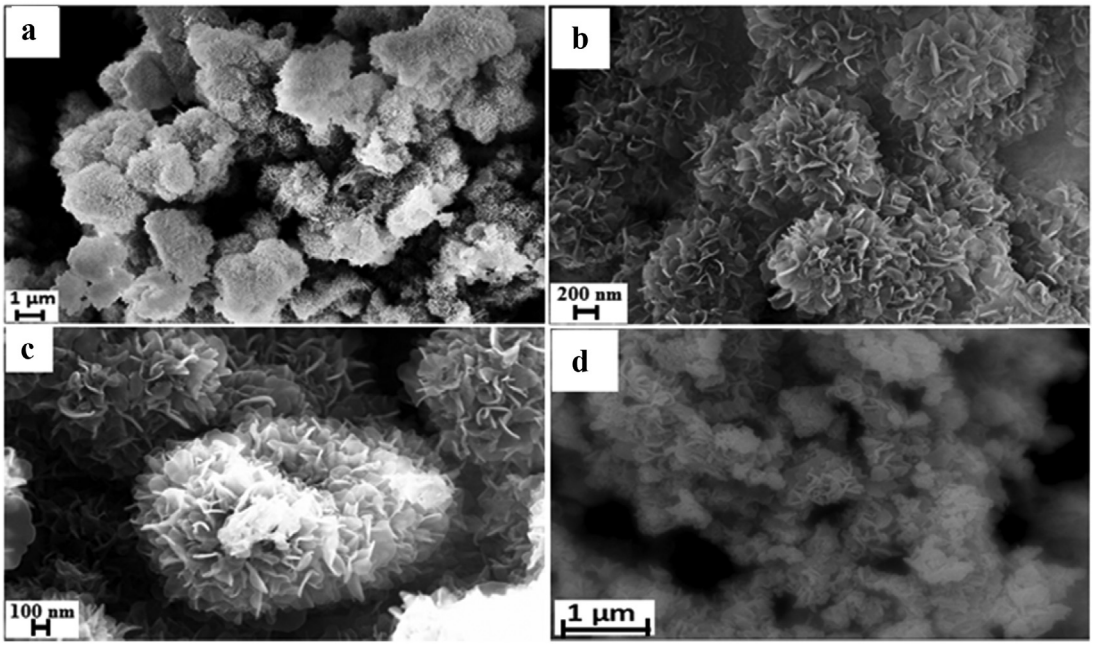

Fig. 1. FESEM image of STNF80 at different magnifications (a and b) and STNF120 (c). The panel (d) shows image of Na-free TiO_2 (anatase) developed by washing the STNF sample.

the hydrothermal reaction, the Na^+ cations residing between the edge-shared TiO_6 octahedral layers could be replaced gradually by water molecules. The size of the water molecules is larger than that of the Na^+ ions; therefore, interlayer spacing is expected to be larger at lower temperatures and the static interaction between neighbouring TiO_6 octahedral is weakened [32,39]. The STNF80C have more water molecules at 80 °C in addition to an incomplete interlayer structure; and therefore, an imperfect nanoflower shape was observed. Increasing the calcination temperature to 120 °C optimized the nanoflower morphology. For Na-free TiO_2 sample (Fig. 1d), the nanoflower structure is slightly modified compared to its Na counterpart. Excessive washing of the STNF samples with water removed the Na^+ ions thereby modifying the morphology even after calcination at 500 °C [39]. The placement of Na^+ ions is important in pinning adjacent layers of nanosheet on the bulk TiO_2 nanoparticles thereby stabilizing the layered structure [29].

Although size of individual flower is rather large (~2.5 μm), the fraction of surface of the sodium titanate nanoflowers is appreciable compared to their volume. The BET specific surface area of the flowers measured from the adsorption studies was ~35 $m^2\ g^{-1}$ with a pore size of ~22 nm and specific pore volume of ~210 $mm^3\ g^{-1}$. The size and morphology of the STNFs are expected to be tunable by varying the synthesis conditions, efforts for which are currently underway.

Fig. 2 shows the XRD pattern of the hydrothermal product as well as that heated at elevated temperatures. All the diffraction peaks of the as-prepared hydrothermal product can be indexed to the orthorhombic $Na_2Ti_2O_4(OH)_2$ phase based on the previous reports [39,40]. The peaks were clearly resolved when the STNF was heated up to 120 °C. The peaks at 2θ = 9.06°, 14.4°, 24.6°, 29.4°, 38.0°, 44.4°, 47.7°, 61.9° and 67.2° correspond to the (2 0 0), ($\bar{2}$ 0 1), (1 1 0), (3 1 0), (0 0 4), (6 0 2), (0 2 0), (0 0 6), and (6 $\bar{2}$ 3) planes of the orthorhombic $Na_2Ti_2O_4(OH)_2$ phase. The XRD patterns suggest that the $Na_2Ti_2O_4(OH)_2$ synthesized in the present study is *a*-axis oriented with lattice parameters a = 18.5 Å; b = 3.1978 Å; and c = 2.9899 Å, which are in agreement with the reported values. The interlayer spacing of the titanate with layered structure is related to the low angle diffraction peak (2θ ~ 9.06°) in the XRD patterns; which for the $Na_2Ti_2O_4(OH)_2$ is calculated to be 0.975 nm. The calcined STNFs retained the layered structure. However, the interlayer spacing is lowered slightly with increase in the hydrothermal temperature, which is probably due to evaporation of crystallized water. The lattice spacing 0.23 nm and 0.35 nm determined by TEM are consistent with that obtained from XRD measurements (peaks at 2θ = 24.6° and 38.0° corresponding to d values of 0.36 and 0.23 nm, respectively). Due to the layered structure, the alkali metal ions are exchangeable with H^+ ions, other metal ions or organic cations [41]. As can be seen for Na-free TiO_2 sample, the diffraction peak at 2θ = 9.0° and 29.4° disappeared due to the exchanging of Na^+ ions with H^+ ions. On the other hand, the peaks at 2θ ~ 24.6° and 47.7° survived the washing condition unlike the peaks at 9.0° and 29.4°. These observations indicate that hydrogen ions could not insert into the vacancies of sodium ions; therefore, the structure was stabilized into anatase crystal structure.

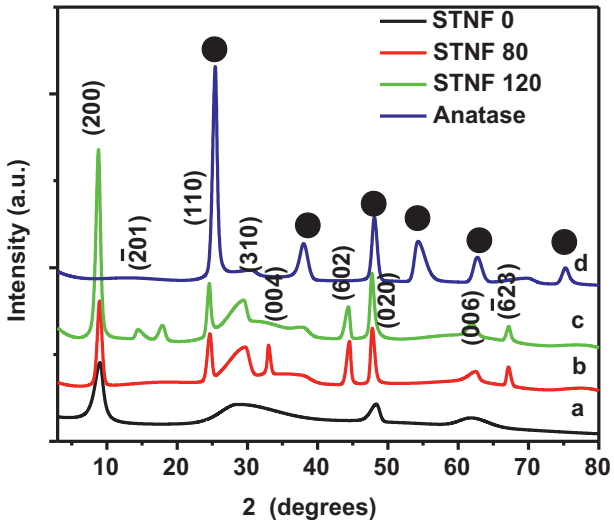

Fig. 2. XRD pattern of STNFs sample (a) washed and dried after hydrothermal reaction, (b) after calcination (STNF80C) at 80 °C, (c) after calcination (STNF120C) at 120 °C, (d) TiO_2 (anatase) developed by washing the STNF. The indices are that of the STNF and the black dots are for the anatase.

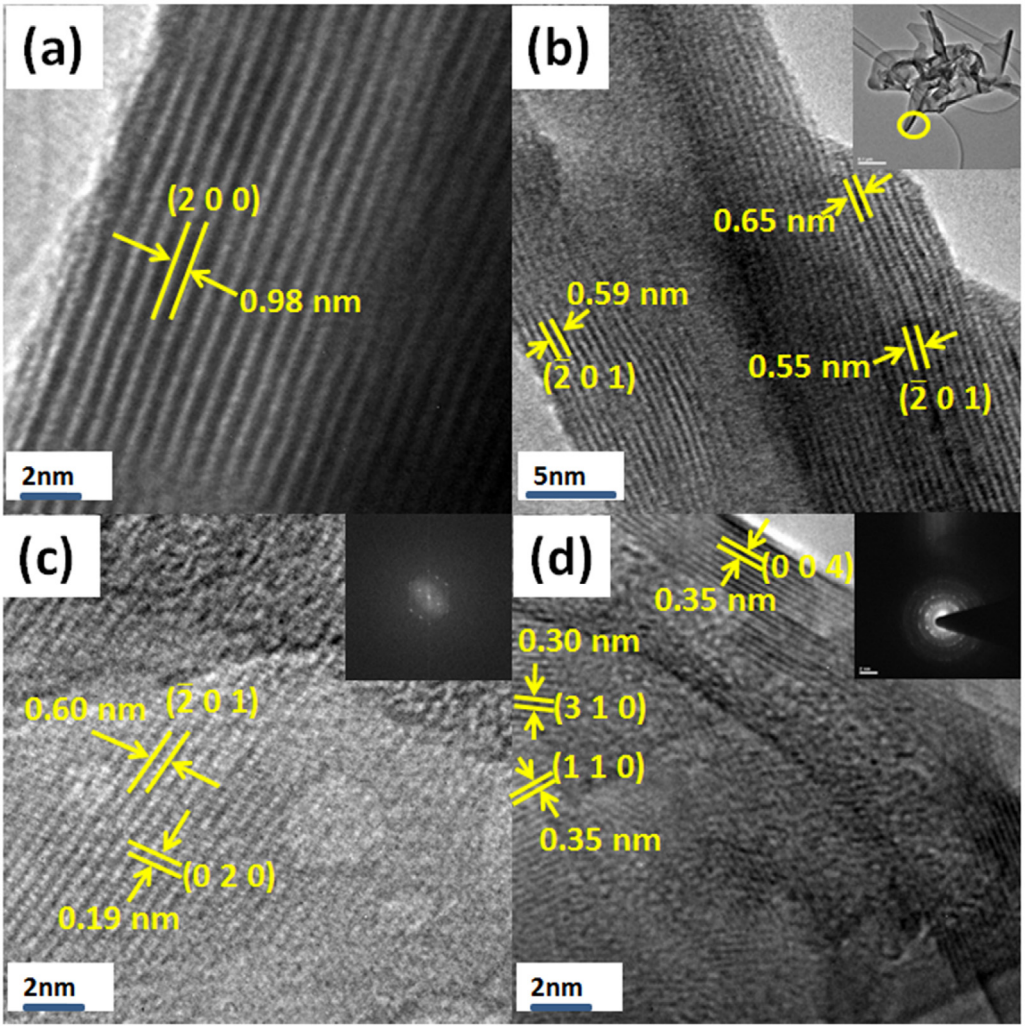

Fig. 3. High resolution lattice images of $Na_2Ti_2O_4(OH)_2$ showing different lattice planes. (a) The (2 0 0) plane showing the interlayer spacing. Inset of (b) is the bright field TEM image from where the corresponding lattice image was recorded. Lattice strain in the ($\bar{2}$ 0 1) plane is indicated in (b). Inset of (c) FFT showing the crystal symmetry. Inset of (d) selected area electron diffraction pattern.

Fig. 3 shows the results of high resolution TEM (HRTEM) studies. Table 1 compares the lattice spacing determined from XRD and HRTEM images. Lattice spacing of all the six planes observed in the HRTEM images closely match with that observed in the XRD patterns. The HRTEM image in Fig. 3a shows an extended periodicity, the lattice spacing of which was found to be 0.98 nm corresponding to the (2 0 0) interlayer plane. The other five planes are shown in Fig. 3b–d, the insets of which show bright field image of a typical nanosheet, fast Fourier transform (FFT), and selected area electron diffraction (SAED) pattern of the respective images. The FFT in Fig. 3c reveals an orthorhombic unit cell consistent with the structure assigned the $Na_2Ti_2O_4(OH)_2$ using XRD patterns. The HRTEM images and the corresponding SAED pattern show that the STNFs are polycrystalline with many crystallites of varying size and orientation. The HRTEM images display changing of lattice spacing along the same array of atoms revealing lattice strains, which are shown to have beneficial influence in their electronic properties. As a typical example, Fig. 3b shows variation in the spacing of the ($\bar{2}$ 0 1) plane, which varies from 0.55 nm to 0.65 within the same grain. Therefore, lattice strain in the present case originated from the flower-like morphology with anisotropic surface profile along similar petals or sheets. The close similarity in the structural details unravelled by the XRD and HRTEM leads us to conclude that the $Na_2Ti_2O_4(OH)_2$ synthesized in this work is single phase and has a layered orthorhombic crystal structure.

Table 1
Comparison of lattice spacing for sodium titanate obtained from XRD and HRTEM analysis.

Crystal Plane	Lattice spacing (nm)	
	XRD	HRTEM
(2 0 0)	0.98	0.98
($\bar{2}$ 0 1)	0.61	0.59 and 0.60
(1 1 0)	0.36	0.35
(3 1 0)	0.30	0.30
(0 0 4)	0.33	0.35
(6 0 2)	0.20	Not observed
(0 2 0)	0.19	0.19
(0 0 6)	1.49	Not observed
($\bar{6}$ 2 3)	1.39	Not observed

Fig. 4a and b shows the CV data of the STNFs and Na-free TiO_2 (anatase) samples in 1 M KOH aqueous solution at room temperature at various scan rates. The use of $Na_2Ti_2O_4(OH)_2$ as an electrode material for electrochemical supercapacitors in mild solutions is based on two different mechanisms; viz. (i) EDLC and (ii) redox reaction in which cations are inserted and extracted from the electrolyte. The enhancement of C_S in STNF is predominantly resulted from the redox process in which the initial process is the reduction

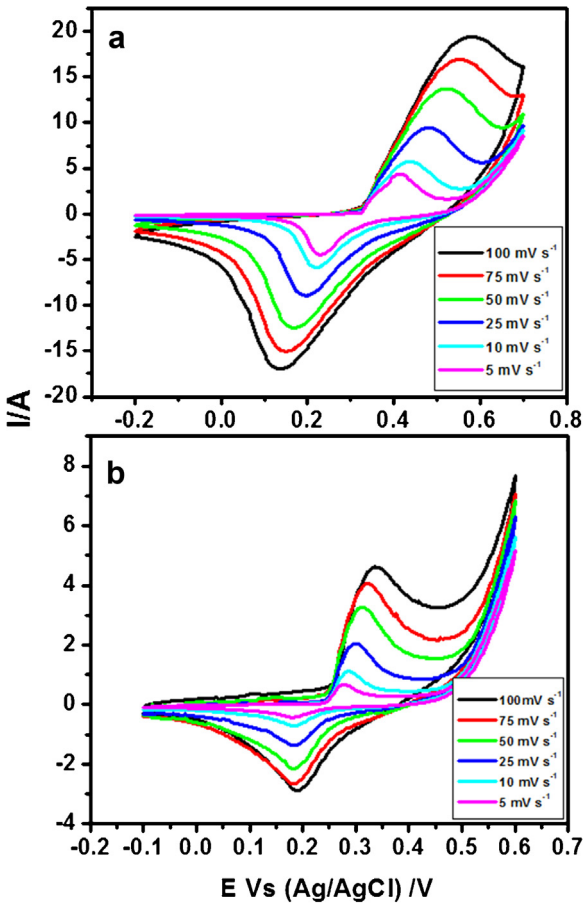

Fig. 4. Cyclic voltammograms of (a) STNF and (b) Na-free TiO_2 at various scan rates in 1 M KOH electrolyte solution.

of $Na_2Ti_2O_4(OH)_2$ to $Na_2Ti_2O_2(OH)_2(OC)_2$, where C is the metal cation (e.g., Li^+, Na^+, K^+). The initial reduction process involve the incorporation of proton/cation and electrons in the $Na_2Ti_2O_4(OH)_2$ lattice. Only thin a layer of the electrode is involved in this reaction; and therefore, this homogeneous process occurs reversibly without any phase changes. The initial reduction reaction is generally described as [42,43];

$$MO_2 + \delta C^+ + \delta e^- \rightleftarrows MOOC_\delta \quad (1)$$

where M is the metal element. When $\delta = 2$, the STNF initial reduction could be represented as

$$Na_2Ti_2O_4(OH)_2 + 2C^+ + 2e^- \rightleftarrows Na_2Ti_2O_2(OH)_2(OC)_2 \quad (2)$$

The CV curves showed corresponding peak potentials at 0.15 V and 0.55 V at a scan rate of 100 mV s^{-1}, which come from oxidation and reduction reaction of STNF thereby indicating the energy storage under pseudo-capacitance mode. The redox reaction at the thin surface of the reduced STNF electrode involving the insertion and extraction of cations could be represented as,

$$Na_2Ti_2O_2(OH)_2 \underset{\text{discharging}}{\overset{\text{charging}}{\rightleftarrows}} Na_2Ti_2O_4(OH)_2 + 2C^+ + 2e^- \quad (3)$$

During charging, oxidation takes place thereby changing the oxidation state of Ti from +3 to +4. The reversible reactions which lead to reduction of STNF occur during discharging.

The observed simultaneous occurrence of these two storage modes, i.e., pseudo-capacitance and electrical double layer, results from its peculiar layered structure. The interlayer distance of the $Na_2Ti_2O_4(OH)_2$ with layered structure is mainly related to the

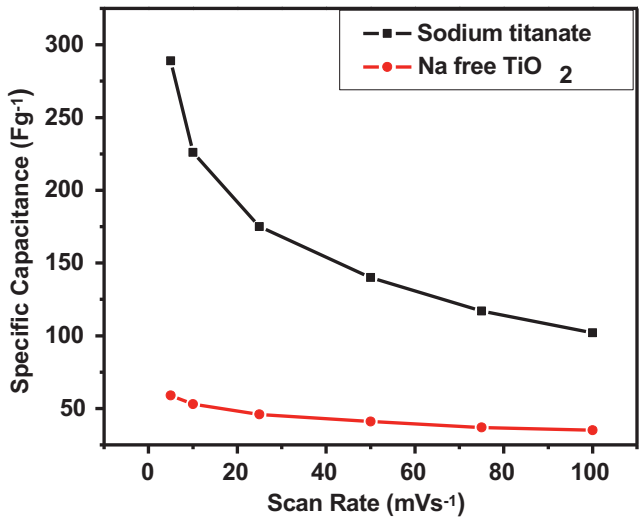

Fig. 5. Variation of specific capacitance of (a) anatase and (b) $Na_2Ti_2O_4(OH)_2$ as a function of scan rates.

low angle diffraction peak ($2\theta \sim 9.06^\circ$) as shown in XRD patterns. Sodium atom is coordinated with water molecules trapped within interlayer space after hydrothermal synthesis which could sustain the stability of layered structure [44]. According to the TEM and XRD analyses, the hydrated layered $Na_2Ti_2O_4(OH)_2$ undergoes a slow reconstruction to form a layered material. Such phase transition process is so slow because water molecules could easily be re-adsorbed into some loose interlayer that remained at lower calcination temperatures [29]. These re-adsorbed water molecules could accelerate cations diffusion thereby increasing the specific capacitance.

The C_S (F g^{-1}) of the samples was estimated from the CV curves according to the following equation:

$$C_S = \frac{1}{2mv(E_2 - E_1)} \int_{E_1}^{E_2} i(E)\, dE \quad (4)$$

where E_1 and E_2 are the cutoff potentials in the CV curves and $i(E)$ is the current at each potential such that $\int_{E_1}^{E_2} i(E)\, dE$ represents total voltammetric charge; m is the mass of the active material, and v is the scan rate. To isolate the supercapacitive performance of the $Na_2Ti_2O_4(OH)_2$ material, a careful electrochemical characterization of the material and a series of control experiments were performed. The background capacitance of Ni foam is evaluated from the area under the CV curve. The area of the CV curve without using the $Na_2Ti_2O_4(OH)_2$ was ~0.00013 cm^2, which is only 0.02% of the total area in the presence of it (see Supporting information, S3), thereby suggesting that contribution from the Ni foam is negligible in our experiment. Fig. 5 shows the variation of C_S as a function of scan rate determined from the CV data. The C_S increased exponentially as the scan rate decreased, typically observed in similar studies [45,46]. Highest C_S observed for the $Na_2Ti_2O_4(OH)_2$ nanoflowers was ~300 F g^{-1} at a scan rate of 5 mV s^{-1}; which to the best of our knowledge is the highest so far achieved for an alkali titanate. As mentioned earlier, the layered structure that facilitated storage employing two modes are responsible for the observed high C_S. To ensure that the enhanced C_S is originated from the layered structure, we undertook similar measurements on the Na-free TiO_2 samples having similar flower morphology. The C_S of Na-free TiO_2 nanoflowers was ~60 F g^{-1}, i.e., lower by a factor of six compared with that of the STNF samples under similar testing conditions. The tiny flower-like structure is likely be one of the alternative ways for improving the performance of energy storage devices. As the

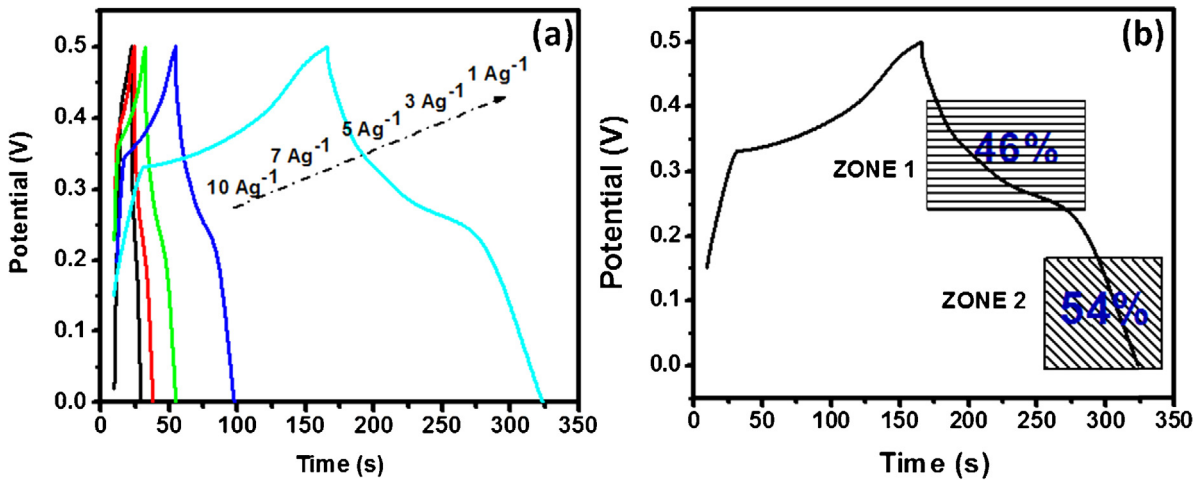

Fig. 6. (a) Galvanostatic charge–discharge for STNF sample at various current densities in 1 M KOH electrolyte, (b) distribution of EDLC and pseudocapacitance contribution to the *CS* value of STNF electrode during charge–discharge cycle at 1 A g^{-1} in 1 M KOH electrolyte.

more layers involve in the reaction, the greater the surface area and capacity to hold on the energy – a feature that is thought to be useful in energy storage devices as well as solar cells.

The supercapacitive performances of the STNF samples were evaluated from the galvanostatic charge–discharge curves in the potential range of 0–0.5 V at different current densities under 1 M KOH electrolyte (Fig. 6a). The C_S could be calculated from a charge–discharge analysis using the relation:

$$C_S = \frac{It}{m\Delta V} \quad (5)$$

where I, t, m and ΔV are applied current, discharge time, active mass, and open potential, respectively. Fig 6a shows that the redox capacitance of flower-like $Na_2Ti_2O_4(OH)_2$ at different current densities of 1, 3, 5, 7 and 10 A g^{-1} were 315, 258, 222, 188 and 136 F g^{-1}, respectively. Obviously, a higher capacitance could be obtained at a lower galvanostatic current condition during a charge–discharge process. The shape of the charge–discharge curves is independent of current density applied thereby indicating that the $Na_2Ti_2O_4(OH)_2$ developed here is suited for its application as an electrode material in supercapacitors. As noted from the CV measurements, the observed C_S has contributions from Faradaic (pseudo) and non-Faradaic (EDLC) process. Relative contribution of these two storage modes was determined from galvanostatic discharge curves. Fig. 6b shows a typical discharge curve categorized into two zones corresponding to pseudo (Zone 1) and EDLC (Zone 2) modes. The contribution of C_S from the Zones 1 and 2 was calculated according to Eq. (5) to be 46 and 54%, respectively. i.e., relatively larger contribution was observed from the non-Faradaic process. In the case of $Na_2Ti_2O_4(OH)_2$ with layered structure, the contribution of C_S in Zone 2 is the sum of EDLC and intercalation capacitance resulting from the layered structure i.e., the layered structure in the material provides more available active sites for charge storage.

The contribution of C_S from the Ni foam substrate was also studied in 1 M KOH from the discharge curves without using the $Na_2Ti_2O_4(OH)_2$ electrode (see Supplementary information, S4). The discharge time was 0.36 s using only Ni foam whereas it was 36 s in the presence of the electrode material; thereby demonstrating the negligible capacitive contribution from the Ni foam.

Stability of electrochemical cycling in the $Na_2Ti_2O_4(OH)_2$ electrode was studied up to 1000 cycles. Fig. 7 shows the variation of C_S as a function of cycle of operation. Two stages of capacitance degradation were observed, viz. ~10% capacitance loss during the initial 200 cycles and a slower degradation of ~5% until 1000 cycles. Fast initial capacitance loss is expected to be contributed from the component from the intercalation. The device was physically stable; no leeching of active material was observed during the cycling tests.

Electrochemical impedance spectroscopy (EIS) measurements were carried out to determine the charge kinetic properties of the device associated with the above supercapacitive parameters. Fig. 8a shows the Nyquist plot of the device in the frequency range of 10,000–0.01 Hz recorded at an applied potential of 0.01 V. This impedance plot is characterized by two distinct parts, a semicircle at high-frequency and a linear line at low-frequency. Inset picture shows a clear semicircle at a high frequency region and a straight line at low frequency region. This semicircle is related to the electrical resistance within the electrode materials and its diameter is related to the charge transfer resistance, denoted as R_{ct}. The estimated R_{ct} value of the $Na_2Ti_2O_4(OH)_2$ is ~0.2 Ω. The equivalent series resistance (ESR) of the $Na_2Ti_2O_4(OH)_2$ electrode in an open circuit condition can be evaluated by determining the intersecting point of the curve at the real axis in the range of high frequency. In this analysis, the ESR of $Na_2Ti_2O_4(OH)_2$ nanoflower is approximated to be ~0.6 Ω. This resistance is also known as bulk solution resistance (R_Ω) and it is composed of three sections; the ionic resistance of electrolyte, the intrinsic resistance of the electro active material, and the contact resistance between the active material and the current collector. This bulk solution resistance

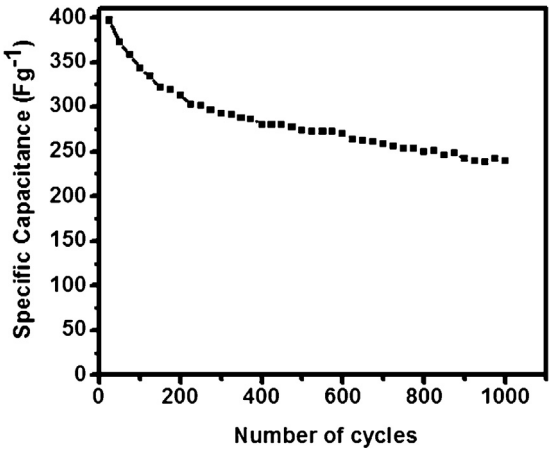

Fig. 7. Galvanostatic charge/discharge cycling behaviour of the STNF electrode at constant charging currents of 3 A g^{-1}.

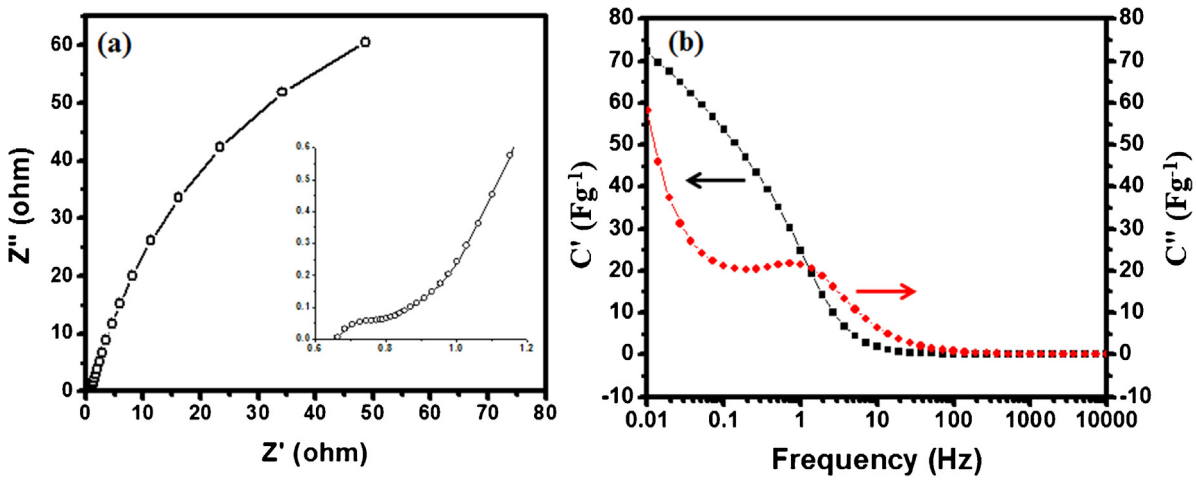

Fig. 8. (a) Nyquist plot of $Na_2Ti_2O_4(OH)_2$ obtained by impedance analysis carried out at potential 0.01 V of employing the supercapacitor device. The inset figure shows shape of the curve in the medium frequency region showing lower resistance, (b) evolution of the real and imaginary part of the capacitance vs. the frequency.

is large with the three electrode system configuration used and would be lower for a two electrode setup with a thin electrolyte layer [47]. The relatively small ESR is expected due to the network structure facilitating the efficient access of electrolyte ions to the $Na_2Ti_2O_4(OH)_2$ surface and shortening the ion diffusion, consequently enhanced the electrochemical properties of the devices. The straight line portion in the medium region of the Nyquist plot is the Warburg resistance resulting from the frequency dependence of ion diffusion/transport in the electrolyte [48]. The larger Warburg resistance indicates greater variations in ion diffusion path lengths and increases obstruction of ion movement. However, Warburg curve is shorter in this study than other reported supercapacitor electrodes [49], which is an indication that the $Na_2Ti_2O_4(OH)_2$ electrode has short ion diffusion may be due to the existence of hydrated layered structure assist the ion diffusion process to the surface of the electrode.

Evolution of the real and imaginary parts (C' and C'') of the electrochemical capacitance obtained from electrochemical impedance spectroscopy (Fig. 8b) was plotted according to following equations:

$$C'(\omega) = -\frac{Z''(\omega)}{\{\omega|Z(\omega)|^2\}} \quad (6)$$

$$C''(\omega) = -\frac{Z'(\omega)}{\{\omega|Z(\omega)|^2\}} \quad (7)$$

where C' represents the real part of the cell capacitance and C'' the imaginary part related to the losses in the charge storage process leading to an energy dissipation. $Z'(\omega)$ and $Z''(\omega)$ are the respective real and imaginary parts of the complex impedance $Z(\omega)$. ω is the angular frequency and it is given by $\omega = 2\pi f$. Relaxation time constant, τ_0 (=$1/f_0$) can be defined as minimum time needed to discharge all of the energy from the sample with an efficiency of greater than 50%, where f_0 is the maxima frequency of the peak [50]. It also can be used determine the electrochemical capacitance retention ability and show the limit between the resistive and the capacitive behaviours [49,51,52]. The relaxation time constant obtained from the peak frequency of $C''(\omega)$ vs. frequency is 1.4 s. This value is comparable with other transition metal oxide electrode of supercapacitor such as $RuO_2{\cdot}nH_2O$ (τ_0 = 1.98 s) [53]. The lower relaxation time constant means that the supercapacitors are able to deliver higher power and reflects a higher percentage of useful capacitive energy [54,55].

4. Conclusions

Sodium titanate hydrate [$Na_2Ti_2O_4(OH)_2$] nanoflowers are synthesized via hydrothermal method without using any templates and characterized. The $Na_2Ti_2O_4(OH)_2$ crystallized in orthorhombic phase with an interlayer spacing of 0.975 nm. The $Na_2Ti_2O_4(OH)_2$ had a flower-like morphology with size ~2.5 μm and are formed by growth of ultrathin nanosheets of size ~20–30 nm from a central zone. Anatase (TiO_2) flowers of similar morphological features are also developed from the $Na_2Ti_2O_4(OH)_2$. The capacitive behaviour of the materials was studied by cyclic voltammetry and galvanostatic cycling. Experiments show that the layered titanate has sixfold higher specific capacitance than the anatase of similar morphology. In the layered titanate, the observed high specific capacitance originated from a combination of electric double layer on account of the interlayer and pseudocapacitance. It is expected that the presence of re-adsorbed water molecules within some loose interlayer plays an important role in assisting the diffusion process of cations as confirmed by the shorter Warburg curve in EIS analysis, consequently giving higher specific capacitance. The knowledge acquired in this study is useful for developing new layered alkali titanates for electrochemical supercapacitors.

Acknowledgements

This work is supported by the Exploratory Research Grant Scheme of Ministry of Higher Education, Govt. of Malaysia on the development of nanostructured materials for efficient energy storage (RDU110602); and Malaysian Technological Universities Network (MTUN) grant on metal oxide semiconductors (RDU 121210).

Appendix A. Supplementary data

Supplementary data associated with this article can be found, in the online version, at http://dx.doi.org/10.1016/j.electacta.2013.09.128.

References

[1] A.S. Aricò, P. Bruce, B. Scrosati, J.M. Tarascon, W. Van Schalkwijk, Nanostructured materials for advanced energy conversion and storage devices, Nat. Mater. 4 (2005) 366.
[2] P. Simon, Y. Gogotsi, Materials for electrochemical capacitors, Nat. Mater. 7 (11) (2008) 845.

[3] G. Wang, L. Zhang, J. Zhang, A review of electrode materials for electrochemical supercapacitors, Chem. Soc. Rev. 41 (2012) 797.
[4] D.W. Wang, F. Li, H.M. Cheng, Hierarchical porous nickel oxide and carbon as electrode materials for asymmetric supercapacitor, J. Power Sources 185 (2008) 1563.
[5] Q. Liu, O. Nayfeh, M.H. Nayfeh, S.T. Yau, Flexible supercapacitor sheets based on nanocomposite materials, Nano Energy 2 (2013) 133.
[6] B. Senthilkumar, K. Vijaya Sankar, C. Sanjeeviraja, R. Kalai Selvan, Synthesis and physico-chemical property evaluation of PANI-$NiFe_2O_4$ nanocomposite as electrodes for supercapacitors, J. Alloys Compd. 553 (2013) 350.
[7] Y.N. Sudhakar, M. Selvakumar, Ionic conductivity studies and dielectric studies of poly(styrene sulphonic acid)/starch blend polymer electrolyte containing LiClO, J. Appl. Electrochem. 43 (2013) 21.
[8] WengF Y.T., C.B. Tsai, W.H. Ho, N.L. Wu, Polypyrrole/carbon supercapacitor electrode with remarkably enhanced high-temperature cycling stability by TiC nanoparticles inclusion, Electrochem. Commun. 27 (2013) 172.
[9] A.G. Pandolfo, A.F. Hollenkamp, Carbon properties and their role in supercapacitors, J. Power Sources 157 (2006) 11.
[10] S. Park, M. Vosguerichian, Z. Bao, A review of fabrication and applications of carbon nanotube film-based flexible electronics, Nanoscale 5 (2013) 1727.
[11] JiangF J., Y. Li, J. Liu, X. Huang, C. Yuan, X.W. Lou, Recent advances in metal oxide-based electrode architecture design for electrochemical energy storage, Adv. Mater. 24 (2012) 5166.
[12] B. Jin, Q. Yan, Y. Dou, Materials for energy storage and conversion based on metal oxides, Recent Pat. Mater. Sci. 5 (2012) 199.
[13] Y. Jun, J.H. Park, M.G. Kang, The preparation of highly ordered TiO_2 nanotubes arrays by an anodization method and their applications, Chem. Commun. 48 (2012) 6456.
[14] N.L. Lala, R. Jose, M.M. Yusoff, S. Ramakrishna, Continuous tubular nanofibers of vanadium pentoxide by electrospinning for energy storage devices, J. Nanoparticle Res. 14 (2012) 1201.
[15] MalinauskasF A., J. Malinauskiene, A. Ramanavičius, Conducting polymer-based nanostructurized materials: electrochemical aspects, Nanotechnology 16 (2005) R51.
[16] Z. Yin, Q. Zheng, Controlled synthesis and energy applications of one-dimensional conducting polymer nanostructures: an overview, Adv. Energy Mater. 2 (2012) 179.
[17] S. Chaudhari, Y. Sharma, P.S. Archana, R. Jose, S. Ramakrishna, S. Mhaisalkar, M. Srinivasan, Electrospun polyaniline nanofibers web electrodes for supercapacitors, J. Appl. Polym. Sci. 129 (2012) 1660.
[18] R.R. Salunkhe, K. Jang, S.W. Lee, S. Yu, H. Ahn, Binary metal hydroxide nanorods and multi-walled carbon nanotube composites for electrochemical energy storage applications, J. Mater. Chem. 22 (2012) 21630.
[19] R.R. Salunkhe, K. Jang, H. Yu, S. Yu, T. Ganesh, S.H. Han, H. Ahn, Chemical synthesis and electrochemical analysis of nickel cobaltite nanostructures for supercapacitor applications, J. Alloys Compd. 509 (2011) 6677.
[20] C. Ge, Z. Hou, B. He, F. Zeng, J. Cao, Y. Liu, Y. Kuang, Three-dimensional flower-like nickel oxide supported on graphene sheets as electrode material for supercapacitors, J. Sol–Gel Sci. Technol. 63 (2012) 146.
[21] Y. Xiao, S. Liu, F. Li, A. Zhang, J. Zhao, S. Fang, D. Jia, 3D hierarchical Co_3O_4 twin-spheres with an urchin-like structure: large-scale synthesis, multistep-spliting growth, and electrochemical pseudocapacitors, Adv. Funct. Mater. 22 (2012) 4052.
[22] X. Zhou, C. Shang, L. Gu, S. Dong, X. Chen, P. Han, L. Li, J. Yao, Z. Liu, H. Xu, Y. Zhu, G. Cui, Mesoporous coaxial titanium nitride–vanadium nitride fibers of coreshell structures for high performance supercapacitors, ACS Appl. Mater. Interfaces 3 (2011) 3058.
[23] Y.K. Hsu, Y.C. Chen, Y.G. Lin, Characteristics and electrochemical performances of lotus-like CuO/$Cu(OH)_2$ hybrid material electrodes, J. Electroanal. Chem. 673 (2012) 43.
[24] M. Casarin, A. Vittadini, A. Selloni, First principles study of hydrated/hydroxylated TiO_2 nanolayers: from isolated sheets to stacks and tubes, ACS Nano 3 (2009) 317.
[25] Y. Ide, Y. Nakasato, M. Ogawa, Molecular recognitive photocatalysis driven by the selective adsorption on layered titanates, J. Am. Chem. Soc. 132 (2010) 3601.
[26] D.S. Seo, H. Kim, J.K. Lee, Hydrothermal synthesis of $Na_2Ti_6O_{13}$ and TiO_2 whiskers, J. Cryst. Growth 275 (2005) e2371.
[27] E. Morgado Jr., M.A.S. De Abreu, G.T. Moure, B.A. Marinkovic, P.M. Jardim, A.S. Araujo, Characterization of Na nanostructured titanates obtained by alkali treatment of TiO_2-anatases with distinct crystal sizes, Chem. Mater. 19 (2007) 665.
[28] D.V. Bavykin, F.C. Walsh, Elongated titanate nanostructures and their applications, Eu. J. Inorg. Chem. 2009 (2009) 977.
[29] H. Zhang, X.P. Gao, G.R. Li, T.Y. Yan, H.Y. Zhu, Electrochemical lithium storage of sodium titanate nanotubes and nanorods, Electrochim. Acta 53 (2008) 7061.
[30] Y. Zhao, J. Jin, X. Yang, Hydrothermal synthesis of titanate nanowire arrays, Mater. Lett. 61 (2007) 384.
[31] C.K. Lee, C.C. Wang, M.D. Lyu, L.C. Juang, S.S. Liu, S.H. Hung, Effects of sodium content and calcination temperature on the morphology, structure and photocatalytic of nanotubular titanates, J. Colloid Interface Sci. 316 (2007) 562.
[32] M. Wei, Y. Konishi, H. Zhou, H. Sugihara, H. Arakawa, A simple method to synthesize nanowires titanium dioxide from layered titanate particles, Chem. Phys. Lett. 400 (2004) 231.
[33] Y.V. Kolen'ko, K.A. Kovnir, A.I. Gavrilov, A.V. Garshev, J. Frantti, O.I. Lebedev, B.R. Churagulov, G. Van Tendeloo, M. Yoshimura, Hydrothermal synthesis and characterization of nanorods of various titanates and titanium dioxide, J. Phys. Chem. B 110 (2006) 4030.
[34] Y. Tang, D. Gong, Y. Lai, Y. Shen, Y. Zhang, Y. Huang, J. Tao, C. Lin, Z. Dong, Z. Chen, Hierarchical layered titanate microspherulite: formation by electrochemical spark discharge spallation and application in aqueeous pollutant treatment, J. Mater. Chem. 20 (2010) 10169.
[35] Y. Tang, Y. Lai, D. Gong, K.H. Goh, T.T. Lim, Z. Dong, Z. Chen, Ultrafast synthesis of layered titanate microspherulite particles by electrochemical spark discharge spallation, Eur. J. Chem. A 16 (2010) 7704.
[36] J.Q. Huang, Z. Huang, W. Guo, M.L. Wang, Y.G. Cao, M.C. Hong, Facile synthesis of titanate nanoflowers by a hydrothermal route, Cryst. Growth Des. 8 (2008) 2444.
[37] H. Peng, G. Li, Z. Zhang, Synthesis of bundle-like structure of titania nanotubes, Mater. Lett. 59 (2005) 1142.
[38] Y. Yoon, D. Shin, D. Kim, K. Lee, S. Kim, Effects of sodium content of titanate nanotubes on lithium battery performance, J. Nanosci. Nanotechnol. 10 (2010) 6206.
[39] J. Yang, Z. Jin, X. Wang, W. Li, J. Zhang, S. Zhang, X. Guo, Z. Zhang, Study on composition, structure and formation process of nanotube $Na_2Ti_2O_4(OH)_2$, Dalton Trans. 20 (2003) 3898.
[40] D.R. Zhang, C.W. Kim, Y.S. Kang, A study on the crystalline structure of sodium titanate nanobelts prepared by the hydrothermal method, J. Phys. Chem. C 114 (2010) 8294.
[41] A. Nakahira, M. Tamai, T. Isshiki, K. Nishio, Synthesis of nanotube from a layered $H_2Ti_4O_9H_2O$ in a hydrothermal treatment using various titania sources, J. Mater. Sci. 39 (2004) 4239.
[42] S.C. Pang, M.A. Anderson, T.W. Chapman, Novel electrode materials for thin-film ultracapacitors: comparison of electrochemical properties of sol–gel derived and electrodeposited manganese dioxide, J. Electrochem. Soc. 147 (2000) 444.
[43] M. Toupin, T. Brousse, D. Bélanger, Charge storage mechanism of MnO_2 electrode used in aqueous electrochemical capacitor, Chem. Mater. 16 (2004) 3184.
[44] E. Morgado Jr., M.A.S. de Abreu, O.R.C. Pravia, B.A. Marinkovic, P.M. Jardim, F.C. Rizzo, A.S. Araújo, A study on the structure and thermal stability of titanate naotubes as a function of sodium content, Solid State Sci. 8 (2006) 888.
[45] D. Yang, Pulsed laser deposition of manganese oxide thin films for supercapacitor applications, J. Power Sources 196 (2011) 8843.
[46] S.G. Kandalkar, J.L. Gunjakar, C.D. Lokhande, Preparation of cobalt oxide thin films and its use in supercapacitor application, Appl. Surf. Sci. 254 (2008) 5540.
[47] M.N. Patel, X. Wang, D.A. Slanac, D.A. Ferrer, S. Dai, K.P. Johnston, K.J. Stevenson, High pseudocapacitance of MnO_2 nanoparticles in graphitic disordered mesoporous carbon at high scan rates, J. Mater. Chem. 22 (2012) 3160.
[48] Y. Wang, Z. Shi, Y. Huang, Y. Ma, C. Wang, M. Chen, Y. Chen, Supercapacitor devices based on graphene materials, J. Phys. Chem. C 113 (2009) 13103.
[49] R. Farma, M. Deraman, A. Awitdrus, I.A. Talib, E. Taer, N.H. Basri, J.G. Manjunatha, M.M. Ishak, B.N.M. Dollah, S.A. Hashmi, Preparation of highly porous binderless activated carbon electrodes from fibres of oil palm empty fruit bunches for application in supercapacitors, Bioresour. Technol. 132 (2013) 254.
[50] D. Pech, M. Brune, H. Durou, P. Huang, V. Mochalin, Y. Gogotsi, P.L. Taberna, P. Simon, Ultrahigh-power micrometre-sized supercapacitors based on onion-like carbon, Nat. Nanotechnol. 5 (2010) 651.
[51] J.A. Lee, M.K. Shin, S.H. Kim, S.J. Kim, G.M. Spinks, G.G. Wallace, R.O. Robles, M.D. Lima, M.E. Kozlov, R.H. Baughman, Hybrid nanomembranes for high power and high energy density supercapacitors and their yarn application, ACS Nano 6 (2012) 327.
[52] Y. Gao, Y.S. Zhou, M. Qian, X.N. He, J. Redepenning, P. Goodman, H.M. Li, L. Jiang, Y.F. Lu, Chemical activation of carbon nano-onions for high-rate supercapacitor electrodes, Carbon 51 (2013) 52.
[53] P.R. Deshmukh, S.N. Pusawale, R.N. Bulakhe, C.D. Lokhande, Supercapacitive performance of hydrous ruthenium oxide ($RuO_2 \cdot nH_2O$) thin film synthesized by chemical route at low temperature, Bull. Mater. Sci. (2012) (BOMS-D-12-00342: To be published).
[54] C. Portet, P.L. Taberna, P. Simon, E. Flahaut, C. Laberty-Robert, High power density electrodes for carbon supercapacitor applications, Electrochim. Acta 50 (2005) 4174.
[55] G. Zhao, N. Zhang, K. Sun, Porous MoO_3 films with ultra-short relaxation time used for supercapacitors, Mater. Res. Bull. 48 (2013) 1328.